



UPPSALA
UNIVERSITET

UPTEC K 20026

Examensarbete 30 hp
Augusti 2020

Additive manufacturing of lunar regolith simulant using direct ink writing

Billy Grundström



UPPSALA
UNIVERSITET

Teknisk- naturvetenskaplig fakultet
UTH-enheten

Besöksadress:
Ångströmlaboratoriet
Lägerhyddsvägen 1
Hus 4, Plan 0

Postadress:
Box 536
751 21 Uppsala

Telefon:
018 – 471 30 03

Telefax:
018 – 471 30 00

Hemsida:
<http://www.teknat.uu.se/student>

Abstract

Additive manufacturing of lunar regolith simulant using direct ink writing

Billy Grundström

In this work, the use of a lunar regolith simulant as feedstock for the direct ink writing additive manufacturing process is explored, the purpose of which is to enable future lunar in-situ resource utilisation. The feasibility of this approach is demonstrated in a laboratory setting by manufacturing objects with different geometries using methyl cellulose or sodium alginate as binding agents and water as liquid phase together with the lunar regolith simulant EAC-1A to create a viscous, printable 'ink' that is used in combination with a custom three-axis gantry system to produce green bodies for subsequent sintering. The sintered objects are characterised using compressive strength measurements and scanning electron microscopy (SEM). It is proposed that the bioorganic compounds used in this work as additives could be produced at the site for a future lunar base through photosynthesis, utilising carbon dioxide exhaled by astronauts together with the available sunlight, meaning that all the components used for the dispersion – additive, water (in the form of ice) and regolith – are available in-situ. The compressive strength for sintered samples produced with this method was measured to be 2.4 MPa with a standard deviation of 0.2 MPa ($n = 4$). It is believed, based on the high sample porosity observed during SEM analysis, that the comparatively low mechanical strength of the manufactured samples is due to a non-optimal sintering procedure carried out at a too-low temperature, and that the mechanical strength could be increased by optimising the sintering process further.

Handledare: Aidan Cowley
Ämnesgranskare: Wei Xia
Examinator: Peter Broqvist
ISSN: 1650-8297, UPTEC K20026

Populärvetenskaplig sammanfattning

Ett av de stora hindren med att skapa mänskliga utposter på andra himlakroppar bortom jorden är den stora kostnaden kopplad till materialtransport; att skicka material från jorden till månen eller Mars för att bygga infrastruktur och bosättningar skulle kräva väldiga resurser. Ett sätt att undkomma detta är att använda de resurser och råmaterial som redan finns till hands på dessa himlakroppar som konstruktionsmaterial. Ett sådant material av intresse för dessa syften är regolit, som är en beteckning på det sten- och grusmaterial som täcker himlakroppar såsom månen och Mars. Materialsammansättningen skiljer sig beroende på varifrån materialet hämtas, och i detta arbete har ett material som efterliknar egenskaperna hos regolit från månen studerats i syftet att utvärdera möjligheten att tillverka föremål i materialet genom additiv tillverkning. Additiv tillverkning – eller synonymt 3D-skrivning – är en beteckning på en stor mängd olika tillverkningsmetoder som har gemensamt att en digital modell av ett föremål används som utgångspunkt för att skapa ett föremål lager-för-lager. En fördel med additiv tillverkning i jämförelse med mer traditionella tillverkningsmetoder är att metoden typiskt erbjuder större designfrihet på komponenter och mindre materialåtgång.

I detta arbete har en metod använts där en blandning görs bestående av regolit, vatten och ett additiv som därefter laddas i en 3D-skrivare för friformstillverkning av föremål. Additivet är ett biologiskt växtbaserat bindemedel som ökar viskositeten på blandningen och ser till att vatten kan blandas med regolit utan att de separerar. Additivet föreslås kunna produceras *in-situ* vid en framtid bas på månen genom fotosyntes, där koldioxid från astronauter används tillsammans med solljus för att producera utgångsmaterialet för additiven. Eftersom vatten – i form av is – samt regolit redan finns på månen, innebär det att den metod som föreslås i detta arbete kan leda till stora kostnadsbesparingar, eftersom endast en begränsad mängd material behöver skickas från jorden då alla komponenter redan finns – eller kan tillverkas – på plats.

Detta arbete visar att den aktuella metoden kan användas för att tillverka föremål i varierande geometriska former. Kompressionstest på tillverkade prover har utförts och testerna visar att materialet uppvisar en relativt låg styrka i jämförelse med andra metoder, vilket kan bero på att sintringen – som är en upphettning av föremål till en temperatur under dess smältpunkt för att öka hållfastheten – utförts vid en temperatur som är för låg för att vara effektiv för detta material. Ifall sintringen istället utförs under mer lämpade förhållanden är det möjligt att materialet skulle uppvisa en högre styrka som motsvarar de krav som ställs på ett byggnadsmaterial.

Table of Contents

| | |
|--|-----------|
| 1. Introduction..... | 1 |
| 1.1. Aim of thesis..... | 3 |
| 2. Background | 4 |
| 2.1. Literature overview | 4 |
| 2.2. Dispersions | 5 |
| 2.3. Sintering | 7 |
| 2.4. Mechanical properties of ceramic materials..... | 7 |
| 2.5. ISRU processing considerations | 8 |
| 3. Experimental..... | 10 |
| 3.1. Materials..... | 10 |
| 3.2. 3D printer | 11 |
| 3.3. Sintering | 12 |
| 3.4. Characterisation | 13 |
| 4. Results and discussion..... | 13 |
| 4.1. Slurry preparation | 13 |
| 4.2. 3D printing..... | 14 |
| 4.3. Sintering | 18 |
| 4.4. SEM | 19 |
| 4.5. Compression testing..... | 22 |
| 5. Conclusions..... | 23 |
| 6. Future work..... | 24 |
| Acknowledgements..... | 24 |
| References | 25 |
| Appendix | 29 |

1. Introduction

A limiting factor for human space exploration is the restricted amount of mass that can be transported into space due to the high cost associated with space travel [1]. Even though this cost is expected to decrease with the further development of reusable launch systems, the cost per transported mass is likely to remain high due to intrinsic limitations in the storage capacity of spacecraft related to the required propulsion mass [2]. The cost associated with sending one pound – approximately 0.45 kg – of mass in orbit has been estimated to be at least \$10000 [3].

In-situ resource utilisation (ISRU) is a way of reducing the amount of material needed to be sent from Earth by instead utilising resources available at the destination during coming missions to the Moon or to Mars; such an example of ISRU is the planned demonstration of oxygen production from atmospheric CO₂ by the Mars rover Perseverance, launched in 2020 by the National Aeronautics and Space Administration (NASA) [4]. Another example would be the use of native construction materials for buildings and infrastructure on the Moon or on Mars. One such material that has attracted significant interest in the context of space exploration is regolith, which is an umbrella term for the compositionally and morphologically heterogeneous surface layer of rock and fine particles on celestial bodies, the use of which has been studied extensively for ISRU applications [1, 2, 5–7]. Regolith could possibly serve as a raw material for construction, thereby significantly reducing the need for material transport from Earth together with the associated cost of such transport.

Additive manufacturing (AM) – or three-dimensional (3D) printing – is a manufacturing process that has raised much interest in the last couple of decades, not the least due to its ability for rapid prototyping as well as the high level of design freedom enabled by the technology compared to traditional subtractive manufacturing (SM) technologies; these and other features makes AM an attractive technology for future ISRU applications in remote locations [8–10]. During the AM process, an object is built in a layer-by-layer fashion. A computer-aided design (CAD) is split into layers by a computer software and exported as a toolpath, typically in the form of G-code, that give instructions to the machine on how each layer should be built. There exists a multitude of different AM technologies, spanning the material categories of ceramic, metallic and polymer materials [11].

Direct ink writing (DIW) – or robocasting – is an AM technology that is based on the selective deposition of a viscous ink by extrusion through a nozzle [12]. In the context of this work, the words dispersion, ink and slurry will be used interchangeably. The ink – typically –

consists of solid particles dispersed in a liquid phase, and it is typically optimised with regards to its rheological properties by the use of additives, especially by modifying the ink to have it exhibit shear thinning behaviour for facilitated deposition [13]. Additional additives may be used to further optimise the properties of the ink such as controlling the flocculation behaviour of the particles. Typical factors to consider when choosing the liquid phase for the ink are availability, its rate of evaporation, as well as its toxicity. Depending on the final use, the 3D printed item, once manufactured, might be further processed, e.g. by sintering.

Combining additive manufacturing together with *in-situ* resource utilisation is an attractive option, as a single technological system might be used to manufacture objects with differing geometries for a wide range of applications. This idea in itself is not new, and a selection of previous research within this area is further explored in Section 2.1. In fact, as may be evident later on, a more likely scenario would be a combination of AM technologies deployed for ISRU, each complimentary, rather than having one system to rule them all. Specifically, this work tries to fill a gap in the research, focusing on the use of an extrusion based additive manufacturing technology – direct ink writing – using a non-toxic dispersion system. The selection criteria for such a dispersion system has in this instance been, in descending order, low toxicity, potential *in-situ* availability, and low technological complexity in order to increase the robustness of the system.

Water was chosen as the liquid phase for this work owing to its non-toxicity and potential availability on the Moon [14]. Sodium alginate (SA) and methyl cellulose (MC), two bioorganic compounds, were both identified at an early stage of this project as possibly suitable binding agents for the dispersion. A scenario is envisioned here where either sodium alginate or methyl cellulose is produced *in-situ* on the Moon by the use of microorganisms and bioreactors, utilising CO₂ exhaled by astronauts [15, 16]. In such a scenario, all the ingredients for the dispersion – regolith, water and binding agent – could be resourced locally once the initial infrastructure has been set up.

As mentioned previously, when faced with the task of manufacturing an object, one has several technologies to choose from depending on their availability and requirements for the final properties of the item. Only within the ‘technology tree’ of additive manufacturing, five different subprocesses can easily be identified for ISRU on the Moon. Figure 1 shows a schematic diagram of some of the available processes when deciding on manufacturing an item. This diagram is not exhaustive, but rather expands on the steps of interest for the process used for this study, i.e. an extrusion based AM process that uses a dispersion with a binding agent that is finally sintered. Therefore, each box in the diagram might potentially be expanded upon

further, even though this is not done here. Still, the diagram will hopefully give the reader a sense of how the chosen process relates to other processes such as subtractive manufacturing, which requires machining, or casting, which requires formwork to mould elements.

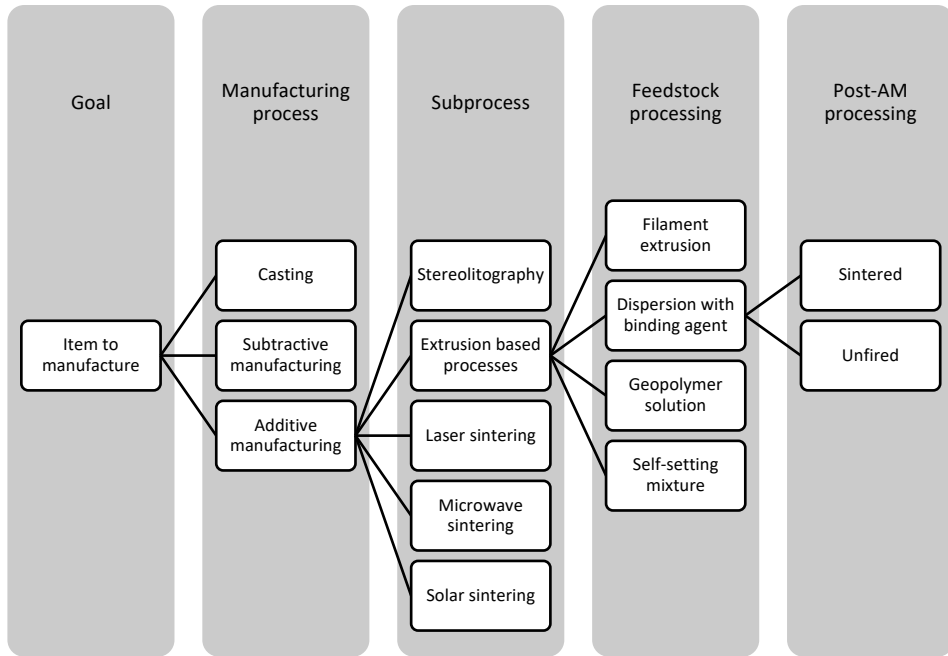


Figure 1. Schematic diagram of a possible decision tree for choosing manufacturing process.

1.1. Aim of thesis

The aim of this thesis is to test the feasibility of the direct ink writing process using a regolith simulant as raw material together with non-toxic additives. More specifically, this work aims to achieve the following:

- To perform a literature study to identify suitable non-toxic additives that are compatible with the DIW process and that also may be produced *in-situ* at a future lunar settlement.
- To formulate a regolith dispersion or ‘ink’ for additive manufacturing using one or more of these additives.
- To identify important process parameters during the AM process and to optimise these parameters based on the properties of the ink to be able to 3D print items out of regolith.
- To characterise the manufactured items by compression testing and scanning electron microscopy (SEM) in order to compare this method with other reported AM methods for ISRU of regolith.

This work was carried out at the European Space Agency (ESA) in Cologne, Germany, as part of an internship at the European Astronaut Centre (EAC).

2. Background

2.1. Literature overview

Table 1 summarises published articles on the use of regolith as a material for additive manufacturing, as well as a minor selection of articles in which casting is used as a production method. It should be noted that test conditions (e.g. geometries, number of replicates and the used standards) for the performed compressive strength measurements vary between sources, which in effect makes a direct comparison of the results of limited use. Still, the compressive strength has been included in the table to give a sense of the current state of each technology. It should also be noted that the availability of actual lunar regolith is highly limited; therefore, research relating to this topic almost exclusively make use of a regolith simulant of terrestrial origin. As these simulants do not share identical properties, it is reasonable to believe that the choice of simulant will have an effect on the results even though this would ideally not be the case.

For the interested reader, an in-depth discussion of additive manufacturing technologies used for space applications is presented in [17]. For a recent discussion of additive manufacturing standards for space applications, refer to [18]. For an extensive review of regolith used in the context of casting technologies, refer to [19]. For a more in-detail discussion of different regolith-binder systems (such as phosphoric acid), refer to [20]. For a discussion of regolith sintering, refer to [21–24]. Compacted regolith as a construction material has been reported in [23–25] and typically display compressive strengths in the range of 100–200 MPa, i.e. an order of magnitude larger than the values reported in Table 1. An instance of stereolithographic AM together with regolith has been reported, but as this article does not provide information on the composition of the photocurable resin, it is not included in the following table [26]. For examples of the use of AM together with other (non-regolith) materials that might be of interest to the reader, such as metal oxides, earth-based materials and clays, that illustrates some of the processing aspects, refer to [8–10, 12, 13, 27–30].

Table 1. Overview of reported use of regolith together with mainly additive manufacturing processes.

DCM = dichloromethane. PLGA = poly(lactic-co-glycolic acid).

| Method | Subprocess | Material | Compressive strength | Year |
|---------|---------------------|--|-------------------------|-----------|
| AM | Binder jetting | Regolith (unknown conc.), Sorel cement, binder liquid | 20 MPa | 2014 [31] |
| AM | Extrusion | Regolith (72 wt.%), urea, alkaline solution | Casted sample: 13 MPa | 2020 [32] |
| AM | Extrusion | Regolith (56 wt.%), phosphoric acid, water | Machined sample: 20 MPa | 2018 [20] |
| AM | Extrusion | Regolith (74 vol.%), PLGA, DCM, plasticizer | 19 MPa | 2017 [22] |
| AM | Extrusion | Regolith (70 vol.%), PLGA, DCM, plasticizer | Not tested | 2017 [33] |
| AM | Laser melting | Regolith | 31 MPa | 2020 [34] |
| AM | Laser melting | Regolith | Not tested | 2016 [35] |
| AM | Laser sintering | Regolith | Not tested | 2019 [36] |
| AM | Laser sintering | Regolith | Not tested | 2016 [37] |
| AM | Laser sintering | Regolith | Not tested | 2015 [38] |
| AM | Laser sintering | Regolith | Not tested | 2012 [39] |
| AM | Microwave sintering | Regolith | Not tested | 2013 [40] |
| AM | Solar sintering | Regolith | 2 MPa | 2018 [41] |
| Casting | Geopolymer | Regolith (76 wt.%), liquid silicate, alkaline solution | 16 MPa | 2015 [3] |
| Casting | Sulphur concrete | Regolith (65 wt.%), sulphur | 31 MPa | 2012 [42] |
| Casting | Thermite reaction | Regolith (67 wt.%), aluminium powder | 18 MPa | 2010 [43] |

2.2. Dispersions

The use of sodium alginate as a binding agent to produce bricks using a clay-water system has been reported, as well as 3D printed structures using earth-based materials together with SA [30, 44]. Alginate is a non-toxic additive used for example in the food industry as a gelling agent to increase the viscosity of food, and a benefit of using alginate over other polysaccharides is that the gelation is not temperature dependant [44]. Alginate has also gained interest as a ‘bio-ink’ owing to its benign biological properties and cell compatibility [45, 46]. Alginates are salts of alginic acid, making up 20–60% of dry algae, with sodium alginate being the salt most used in the industry [44].

Cellulose and its derivatives – such as methyl cellulose – have also been studied for 3D printing applications by virtue of their properties, such as exhibiting shear thinning behaviour, and for their proven use as an additive in construction materials, and also for their availability as an industrial waste product [13]. Cellulose itself is insoluble in water, with methyl cellulose being a functionalised derivative that makes it soluble in aqueous solutions. Carbohydrates such as cellulose consists of monosaccharide units connected by glycosidic linkages. The β -glycosidic linkages of cellulose promote the formation of intermolecular hydrogen bonds between cellulose molecules, giving rise to its linear structure. This chain-like structure is the reason why cellulose is insoluble in water, and also why cellulose functions well as a structural

material [47]. It is these inter- and intramolecular interactions that act against flow in the dispersion which gives rise to the observable increase in viscosity upon addition of additive [48]. Generally, longer molecular chain lengths leads to an increase in viscosity as entanglements between chains in the dispersion increases, which in turn decreases the tendency of the liquid to flow.

The mechanisms of how SA and MC respectively induces gelation differ. Where MC increases the viscosity of the dispersion by introducing long molecular chains that interact through hydrogen bonds as discussed above, SA works by a mechanism that is referred to as the egg-box model in the literature [44, 49]. SA is a block copolymer, where the monomer units are β -D-mannuronic acid (M) and α -L-guluronic acid (G) residues. G-blocks selectively binds to divalent cations present in the solution (preferably Ca^{2+}), closing in around the cation as an egg in a box (the cation being the egg) which give rise to cross-linked chains and an observed increase in viscosity. The ratio of M- to G-blocks in sodium alginate can vary greatly – in one study as much as between 0.23 and 1.04 in five analysed samples [44] – and this will in turn affect the gelling kinetics of the additive. This is of importance to this work, as the contribution to viscosity from methyl cellulose will depend on its molecular weight, while the contribution to viscosity from sodium alginate will depend on its composition, which in turn depends on the source of the material and factors such as growth conditions. Today, alginates for industrial use are extracted from algal sources, but microbial fermentation offers another route for production, making it possible to tune the composition of sodium alginate with regards to M- and G-blocks which might prove to be necessary for critical applications to reduce risks associated with batch variations [49].

Of importance to the properties of the slurry is also how well its particle are distributed and dispersed throughout the matrix. Good distribution means that the particles are evenly spread out, while dispersion is a measurement of how well the particles are separated from each other [48]. Ideally, a system is both well distributed and dispersed. A way to improve the particle dispersion in a slurry is the use of a dispersant, even though such one was not used here. Acetic acid has reportedly been used as a dispersant for ceramic direct ink writing to ensure uniformly well-dispersed solutions and to counteract sedimentation of the ink [50]. It has been suggested that lowering the dispersion pH may reduce electrostatic repulsion between the polymer chain of the additive and the ionic species associated with the solid phase, which in turn would promote adsorption between the two throughout the dispersion [44]. Acetic acid is relatively non-toxic and widely available, and could potentially be produced *in-situ* through microbial fermentation of food waste, making it an interesting dispersant candidate to be investigated in

future work. The use of a dispersant may also be beneficial for the subsequent sintering stage, as formed aggregates in the sample may otherwise lead to a decrease in particle packing, which in turn lowers the efficiency of the sintering process [51].

2.3. Sintering

The major motivation for sintering is to achieve densification and to improve the mechanical properties of the sample. Before a green body – the unsintered object – is sintered, the particles are only weakly held together. During sintering, the particles fuse to each other during a neck formation process, as solid-state mass transport – the mechanism for densification – take place between the particles [51]. The thermodynamic motivation for this process is the decrease of the total surface energy of the system by a decrease in the particle surface area. Finer particle sizes will lead to an increased sintering driving force, as the surface area to volume ratio is larger for these particles [51]. The sintering start for a regolith simulant with particle size less than 20 μm has been reported to be 1066 °C, while a coarser fraction with particle size specified as less than 100 μm required 1091 °C [21].

In addition to particle size, the powder properties of most importance for sintering are particle shape and particle packing. Particles of irregular morphology have high surface area to volume ratio which will increase the driving force for sintering. Increased particle packing will increase the number of contact points between particles, which facilitates sintering as solid-state mass transport is comparably slow process. Indeed, the presence of a liquid phase will speed up mass transport during sintering, meaning a faster densification of the sample [51]. Liquid phase sintering for a regolith simulant has been reported at temperatures above 1060 °C for particle sizes less than 20 μm [21].

2.4. Mechanical properties of ceramic materials

The measured fracture strength of ceramic materials is lower than what can be theoretically anticipated due to flaws in the material acting as stress raisers, some examples of which include surface or interior cracks, internal pores and grain corners [52]. Ceramic materials may have covalent bond which are strong bonds giving rise to a limited number of slip systems compared to other materials such as metals, and may also have ionic bonds, where ions with the same charge repulse each other as they come in close contact. As for the compressive strength of ceramic materials, pores will reduce the actual cross-sectional area of the object, which in turn

weakens it as the load will be applied on a smaller area, causing an increase in pressure P according to:

$$P = \frac{F}{A} \quad (1)$$

where F is the magnitude of the force and A is the contact area.

To illustrate the effect of flaws on the mechanical strength of ceramic materials with a brittle failure mode, one can use the plane strain fracture toughness K_{IC} , which is defined as:

$$K_{IC} = Y \cdot \sigma \cdot \sqrt{\pi \cdot a} \quad (2)$$

where Y is a dimensionless parameter that depends on specimen and crack geometries, σ is the applied stress, and a is the length of a surface crack, or half the length of an internal crack; the parameter a can also be interpreted as the flaw size [52]. Crack formation and propagation will not occur as long as the right hand side of the equation is less than the plane strain fracture toughness of the material. K_{IC} is typically increased with decreasing grain size, and also by decreasing the number of flaws in the material. To achieve a high performing ceramic material, it is thus of outmost importance to reduce the presence of flaws.

2.5. ISRU processing considerations

Adapting the approach presented in this work for ISRU in a lunar environment would of course not be without its challenges, some of which will be discussed here.

One challenge relates to the sintering behaviour of materials in microgravity. It has been reported that sintering in microgravity resulted in less densification and increased porosity of samples compared to samples sintered on Earth, meaning that sintering in microgravity leads to mechanically weaker components as the gravitationally facilitated densification processes and grain compression does not occur to the same degree [23]. On the Moon, the gravitational acceleration is approximately 1/6 of that on Earth, and it is not known how this compares to sintering in microgravity. On the other hand, as the gravity on the Moon is less than on Earth, lunar structures might require less mechanical strength compared to terrestrial structures used for the same purpose.

Another factor to consider is the heterogenous nature of regolith material, and that the exact composition, particle size distribution and particle morphology depends on sampling site (such as the highlands or lunar mare) [1] and it is reasonable to assume that the material needs to be homogenised before it is used as feedstock for other processes to reduce variations in

material properties between batches [18]. It would furthermore be beneficial if the regolith processing steps were carried out without human involvement to reduce the risks associated with dust exposure. For the direct ink writing AM process as it is described here, it is suggested that the production of objects and the subsequent sintering take place in a pressurised environment to control the water evaporation from the samples in such a way that the water may be let to condensate for reuse in the process as liquid phase. A decision would also have to be made with regards to if the sintering should be carried out using electrical heating elements, as in this work, or if another process such as solar sintering should be used instead, with the latter process likely to be more energetically favourable (possibly at the expense of process control).

As discussed previously, alginates are mainly extracted from algal sources. This would be beneficial for ISRU applications, as algae could be produced through photosynthesis by using CO₂ exhaled by astronauts together with sunlight to produce both O₂ and the alginate material that is used as binding additive for the DIW process. Another option is the already mentioned route of microbial fermentation for production, which would be beneficial as this allows for the ability to tailor-make alginates with specific monomer compositions [49]. Cellulose may be extracted from plants in a similar way to how alginate is extracted from algae, and then be functionalised to be water soluble.

A benefit of using a high-resolution AM method such as the one described in this work is that the design flexibility allows it to be used to create moulds of custom design and shape, that in turn can be used for pressing powdered regolith (e.g. creating ‘regolith bricks’) to achieve higher compressive strengths than what is otherwise typically achieved with AM processes as highlighted previously in Section 2.1.

A benefit of using the DIW method as it is described here is that it might bring with it savings in costs associated with establishing a lunar settlement. For the D-shape binder jetting AM technology as described in [31], 3.8 tons of dry salts are required to produce 6 m³ of habitat structure, equalling a living volume of 40 m³. In comparison, if the binding agents investigated in this study are used, this would require 664 kg of additive based on the assumption that the manufactured object has a density of 1661 kg/m³ and that 1 wt.% additive is used. This equals 17% of the payload mass for the D-shape technology, or a cost reduction of \$9 million under the assumption that 1 kg cost \$20000 to transport to the Moon and that water is resourced *in-situ* but not the additives for each process.

3. Experimental

3.1. Materials

EAC-1A, a lunar regolith simulant developed by ESA, has been used for this work. The material composition in wt.% as reported in the literature [6] is summarised in Table 2.

Table 2. Chemical composition of the lunar regolith simulant EAC-1A in wt.%.

| Oxide | wt.% |
|--------------------------------|-------|
| SiO ₂ | 43.70 |
| Al ₂ O ₃ | 12.60 |
| Fe ₂ O ₃ | 12.00 |
| MgO | 11.90 |
| CaO | 10.80 |
| Na ₂ O | 2.90 |
| TiO ₂ | 2.40 |
| K ₂ O | 1.30 |
| P ₂ O ₅ | 0.60 |
| MnO | 0.20 |
| Total | 98.40 |

The grain size for the material range between 0.02–1.0 mm [53]. A sieved fraction with grain size of less than 200 µm was also available for experiments, but the supply was temporarily limited and the majority of the tests were carried out using the fraction with a wider grain size distribution.

Two dispersions were prepared by mixing ingredients according to the ratios given in Table 3, with ‘LA’ referring to ‘Low Additive’ content and ‘HA’ referring to ‘High Additive’ content respectively; HA samples had an increased concentration of additive by a factor of 3.6. Dispersions were prepared using either methyl cellulose ($M_w = 160000$ g/mol) or sodium alginate (both Carl Roth GmbH + Co. KG, Germany) as additive. Regolith simulant was mixed with the powdered additive, to which de-ionised water was then added. The mixture was hand stirred for at least 5 minutes using a mortar and pestle. The resulting dispersion was transferred to a 60 ml syringe for immediate use. After finishing a print, the resulting items were left to dry under ambient conditions for 72 h before sintering.

Table 3. Dispersion content as component mass/EAC-1A mass ratio. LA = Low Additive. HA = High Additive.

| | EAC-1A | Water | Additive |
|----|---------------|--------------|---------------------|
| LA | 1 | 0.40 | $5.6 \cdot 10^{-3}$ |
| HA | 1 | 0.45 | $2.0 \cdot 10^{-2}$ |

3.2. 3D printer

An overview of the key components of the 3D printer used in this work is given in Figure 2. The custom unit is controlled through a controller board which has a graphical user interface and that runs a modified version of the Marlin firmware. The X- and Y-axis (lateral axes) are belt driven by stepper motors connected to microstep drivers for current regulation and step size control. The Z-axis (vertical axis) is a rack and pinion system driven by a stepper motor, on which the extruder subunit can be mounted. The extruder has a stepper motor which actuates a leadscrew with a custom plunger attached to its end which fits into a 60 ml syringe with a 28 mm chamber diameter. The slurry is loaded into the syringe and extruded onto a ceramic build plate. The 3D printer takes G-code files as input which describes the toolpath of the printhead and extruder unit. For this project, a Python file was prepared that generates G-code for a selection of different test geometries, which is available in the Appendix to this work.

The movement speed for the X- and Y-axis was set to 7 mm/s and the extrusion speed was set to 4 μm per mm X and Y travel, which corresponds to 28 $\mu\text{m}/\text{s}$ or a volumetric flow of 17 mm^3/s . The system parameters of importance are listed in Table 4.

Table 4. System parameters for the custom 3D printer.

| Syringe volume | Nozzle diameter | X, Y movement speed | Extrusion speed | Volumetric flow | Layer height |
|-----------------------|------------------------|----------------------------|---------------------------|---------------------------|---------------------|
| 60 ml | 2 mm | 7 mm/s | 28 $\mu\text{m}/\text{s}$ | 17 mm^3/s | 1.2 mm |

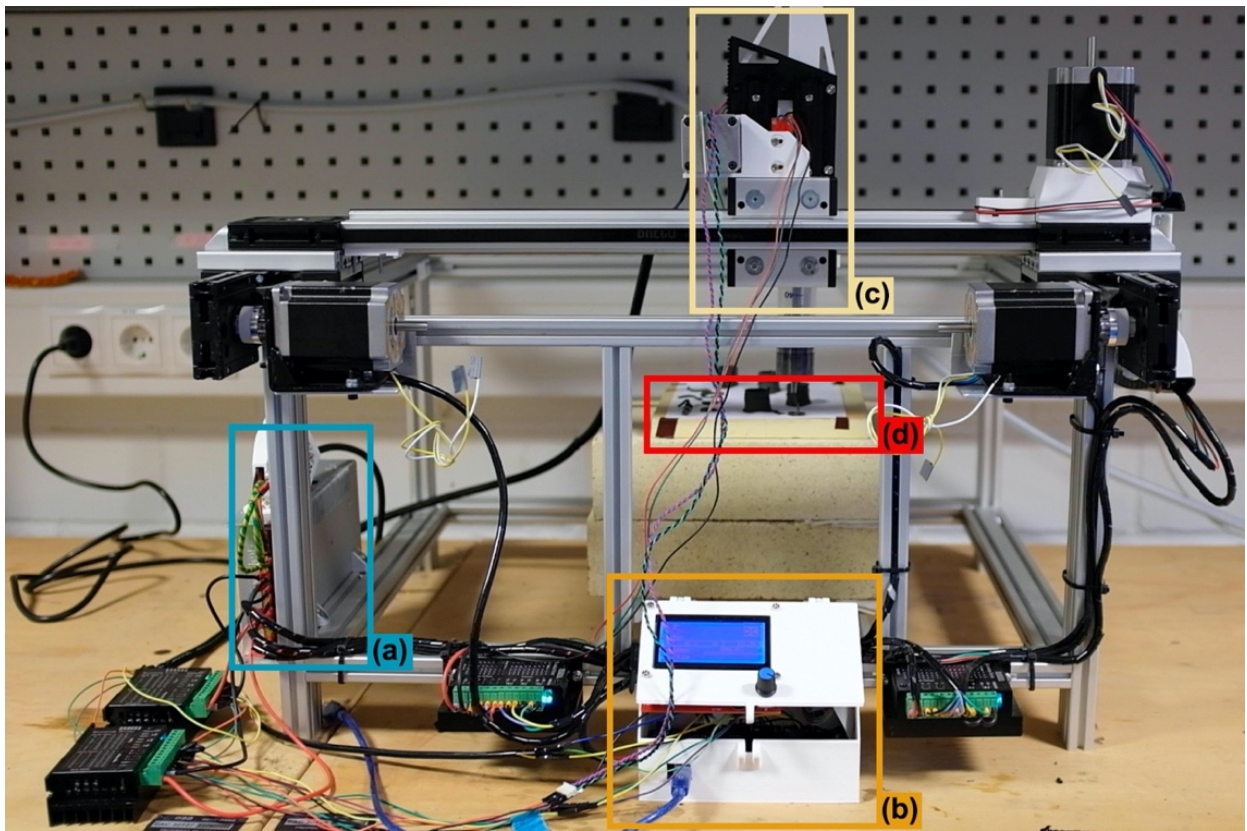


Figure 2. Custom 3D printer overview: (a) power supply unit, (b) controller board with SD slot and graphical user interface, (c) Z-axis and extruder, (d) ceramic build plate.

3.3. Sintering

The sintering was carried out using a Paragon SC-Series 1680 W Kiln with a specified max. temperature of 1093 °C, with an actual max. temperature varying around 1080 °C during sintering. The sintering was carried out over three steps, listed in Table 5, and the kiln was afterwards left to cool to room temperature over a time period of approximately 2 h. The total process took approximately 8.5 h from start to finish.

Table 5. Sintering steps.

| Step | Target temperature | Heating rate | Holding time |
|-----------|--------------------|--------------|--------------|
| Drying | 120 °C | 5 K/min | 45 min |
| Debinding | 500 °C | 5 K/min | 45 min |
| Sintering | 1080 °C | 10 K/min | 120 min |

3.4. Characterisation

A Hitachi TM-1000 scanning electron microscope with an accelerating voltage of 15.0 kV was used for this work. A Shimadzu AGX universal testing machine with a speed setting of 1 mm/min was used for the compressive testing.

4. Results and discussion

4.1. Slurry preparation

When only regolith and water are mixed, the mixture separates into its solid and liquid components as regolith lacks the cohesiveness of clay materials, meaning that water itself is not sufficient to create a self-supporting and extrudable slurry. By using methyl cellulose or sodium alginate as binding agent, the viscosity of the dispersion is markedly increased as the additive comes in contact with water, and the dispersion may be modified from being water-like with high flowability, to being a thick, nonflowing paste, by altering the concentration of additive. Both SA and MC behaves in similar way in this study when compared to each other, resulting in an apparent viscosity similar to each other when each is used at the same concentrations. In a shear thinning liquid, such as one that is ideally used for 3D printing application, an increase in the strain rate will lead to a decrease in viscosity. Both SA and MC slurries reportedly exhibit this behaviour [8, 45].

There was an observed increase in ‘rigidity’ of an extruded strand of dispersion during this work as the concentration of additive is increased; an extruded segment of the higher additive ‘HA’ concentration dispersion resists attempts of indentation with a sharp object when the lower additive ‘LA’ concentration does not do so. It is possible that this increase in observed rigidity of an extruded segment counteracts the interaction and bonding between layers, which might introduce anisotropy in the material similar to what is commonly observed in thermoplastic 3D printing due to the reduced bonding strength *between* layers, compared to *within* layers [54]. As a result of this, it is here suggested that a higher concentration of additive will result in weaker structures if a certain threshold value of additive is surpassed due to reduced interaction between layers, even though this is yet to be confirmed by mechanical strength measurements.

Mixing is an important step to ensure a well dispersed slurry, and the use of a ball mill instead of mortar and pestle might improve the distribution and dispersion of particles in the slurry, especially at higher concentrations of additive, as it was noted during this work that it

was difficult to homogenise a material with the viscosity of a thick paste. Using a ball mill might also be a good way to homogenise the regolith material and decrease the particle size of the material; it has been suggested elsewhere that the ratio of nozzle size to maximum particle diameter should be 10, which equals particles with a maximum size of 200 µm for a 2 mm nozzle as the one used here [30]. As already mentioned, the particles used in this work range between 0.02 and 1 mm in diameter (before mixing) which might lead to a non-optimal flow behaviour.

4.2. 3D printing

The prepared dispersions proved to be extrudable using the 3D printer system available for this work. Experiments using higher concentrations of additive than those reported here were also conducted, but the stepper motor of the extruder unit failed to push the syringe plunger as the dispersion became too viscous, indicating a too low torque on the stepper motor for this application. Similarly, tests were performed using finer nozzle sizes (0.8 mm and 1.2 mm) in combination with the sieved fraction EAC-1A, with the result that the system again was not able to extrude the dispersion. This indicates that the setup would benefit from having the stepper motor upgraded, as the feature size of printed items will depend on the nozzle size, meaning that a finer nozzle enables higher resolution.

Another factor of importance is that printed item exhibit a high green strength to support the subsequent layers as they are deposited. Figure 3 displays a printed hollow cylinder that is approximately 20 mm tall, consisting of 15 layers, where SA was used in low concentration ('LA'). This object demonstrates that the prepared dispersion has enough shape retention to carry its own weight at this scale. The cylinder is not perfectly straight, but it is not certain if this is due to self-buckling of the structure, small inaccuracies in the movement of the printhead, or to slight deviations in how the dispersion expand and contract after extrusion, which, as the print progresses, may lead to dimensional inconsistencies.

It has been reported that a difference of only 2 vol.% in solid loading for a ceramic dispersion can have significant impact on the buckling behaviour of the ink [50, 55]. Considering this, it would be wise to systematically evaluate the limits in solid loading in future works to avoid any self-buckling tendencies of the ink.



Figure 3. 3D printed hollow cylinder consisting of stacked circles (scale bar: 10 mm).

Figure 4 shows a 3D printed lattice structure after sintering, the dispersion used being low additive ('LA') with SA as binder. As is evident from this figure, the structure has collapsed at the unsupported sections of the structure, creating a defect along the side that progressively worsen. However, this collapse has had little influence on the actual inner grid structure which still retain its shape relatively well as seen in the figure. It should be noted that for the commonly used thermoplastic fused filament fabrication (FFF) process, overhangs exceeding 45° are generally not printed without the use of a support structure, and it should therefore not be surprising to observe that the dispersion used here is unable to support 90° overhangs. If a finer grid had been printed, it is possible that the structure would be able to support itself, as can be observed at certain places in Figure 4.

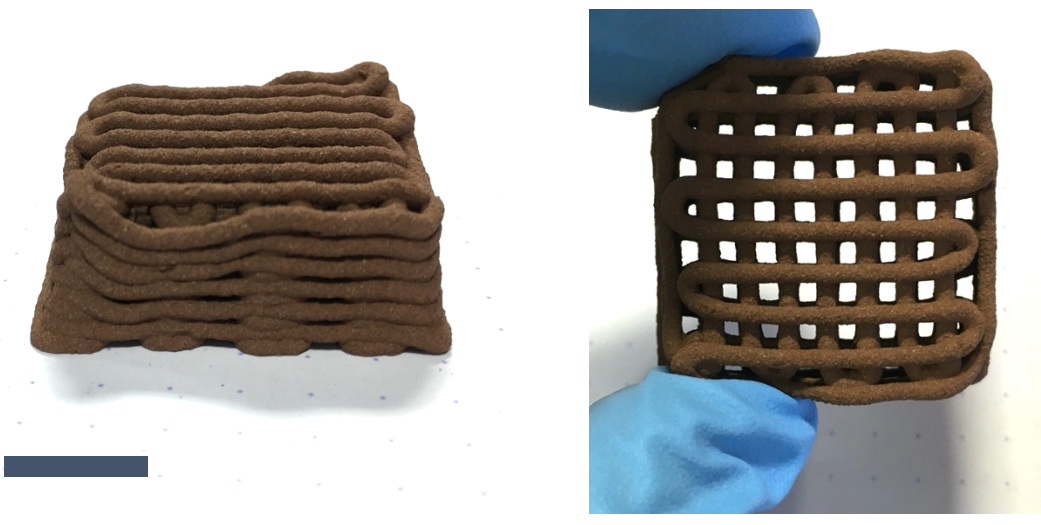


Figure 4. Sintered lattice structure with a grid size of approximately 2.5 mm:
(a) from side, (b) from top held by hand (scale bar: 10 mm).

Figure 5 depicts a 3D printed cylinder that is 33.8 mm tall created with the ‘LA’ dispersion using SA. As demonstrated by this structure, solid objects exhibit structural integrity both during and after a print. The gaps seen at the top is believed to be due to dispersion shrinkage after deposition as water evaporates, and a way to compensate for this would be to use a line width during printing that is slightly less than the nozzle diameter, e.g. 1.8–1.9 mm instead of the 2 mm used here.



Figure 5. Sintered cylinder of 33.8 mm height (scale bar: 10 mm).

An observation when using the ‘HA’ concentration of sodium alginate, printing a set of rectangular objects, was that a crack evolved for all the objects along the same direction on the underside of the objects that is in contact with the ceramic build plate. These cracks were noticed after the drying period of 72 h, and it is therefore not known when they developed as the underside of the samples were not visible until the objects were turned, but it is hypothesised here that the cracks were induced by the drying of the samples.

A possible explanation for this behaviour is that the outer surface of the objects – the surface that is in contact with the ambient air – will dry at a higher rate than the inside of the objects. As water evaporates, the volume of the item will decrease, and this shrinkage will be more pronounced at the outer edges of the samples. If the object is relatively stiff, as noticed when using the ‘HA’ concentration, the parts of the sample with a less pronounced shrinkage (i.e. the inner regions) will ‘resist’ this shrinkage, and the tension that is formed in the sample will give rise to the observed crack. This is presented schematically in Figure 6. No cracks were observed in samples prepared using the ‘LA’ concentration, and it is believed that the reduced stiffness

or rigidity of the ‘LA’ concentration creates less build-up of tension in the samples during the drying process compared to the ‘HA’ concentration, or that the tension is more easily dissipated in the ‘LA’ concentration samples. Another explanation could be the difference in liquid-to-powder-phase ratio between ‘LA’ and ‘HA’ concentrations, as this will affect the capillary action – i.e. the transport of the liquid phase – and porosity in the material. In any case, this observation suggests that there is an upper limit to the amount of additive that should be used, which is below the value where the dispersion still shows good printability during the AM process as was the case for the high additive concentration slurry used here.

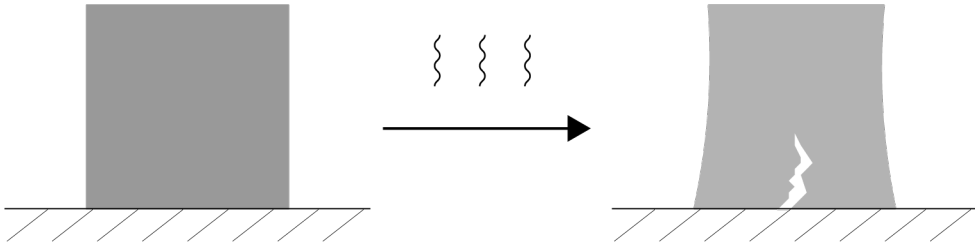


Figure 6. Schematic diagram of how the evaporation process might induce cracks in the high additive concentration samples. Note that the shape deformation due to evaporation is exaggerated in this figure.

It is likely that the direct ink writing process – due to the use of a liquid phase – inevitably will produce relatively loose-packed samples, at least when comparing to other green body preparation processes such as compaction through an external force, and there is a risk that this porosity will have a detrimental effect on the sintering step. This might be mitigated by trying to reduce the non-solid mass of the slurry as much as possible, i.e. by optimising the dispersion with regards to a low water content. Still, dense ceramic bodies have been reported for the DIW process [55].

For all the manufactured objects in this work, the G-code was generated using a custom Python script as mentioned earlier. An obvious advantage over this would be using a fully functional slicer software that accepts CAD files to create more complex geometries. The reason why this is not done here is that no slicer software was found that supports the low extrusion speed that is used for this system; most slicer software are designed for thermoplastic FFF printing (or stereolithographic AM) which typically use extrusion speeds that are several orders of magnitude larger than what is used here, with no or limited possibility to control the value – at least not at the level that is needed. However, the fact that such software was not found within the scope of this project does not mean that there is no such software available.

4.3. Sintering

Figure 7 show the same 3D printed solid cylinder before and after sintering, using the ‘LA’ dispersion and SA as additive. There is little observable difference between the two, with the noticeable exception of hematite formation which takes place during sintering in an oxygen rich environment, giving rise to the observed reddish-brown colour [21]. If regolith is sintered under oxygen deprived conditions – e.g. vacuum – the objects retain their greyish colour [22].

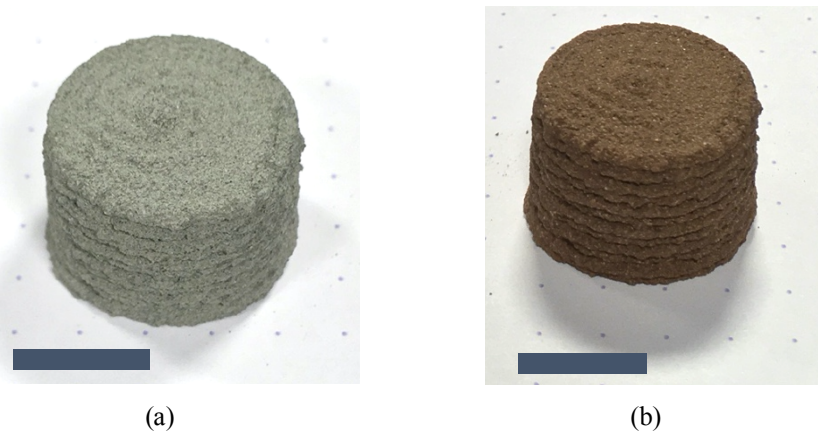


Figure 7. Solid cylinder: (a) before sintering, (b) after sintering (scale bar: 10 mm).

No significant densification of the samples were observed in this work as the items retain most of their initial volume after sintering. Small dimensional deviations in the sample made it difficult to determine its volume with a sufficient degree of accuracy when using a hand measuring tool; otherwise, if the volume was known, it would be possible to determine the degree of densification during sintering.

A comparison that was performed of the mechanical strength between a sintered and a unsintered sample under compression with a hand tool suggests that the strength of the sintered sample is only slightly higher than that of the unsintered sample; however, this is yet to be confirmed through proper measurements. An explanation for this could be a less-than-optimal sintering process; it might be tempting to attribute the colour change of the samples as a sign of successful sintering, but hematite formation is already significant at temperatures around 850 °C, well below the reported sintering start at 1091 °C for particles with a diameter of 100 µm or smaller [21]. As the sintering temperature reached for this work – 1080 °C – is less than the reported sintering start – and also considering that the grain size distribution for the samples prepared in this work range between 20–1000 µm, i.e. containing particles larger than 100 µm – it is reasonable to believe that the sintering was limited in its effect, if it even took

place at all. Considering this, a comparison of the mechanical strength of unsintered samples, the samples prepared here, and samples sintered at a higher temperature could provide useful information about the sintering behaviour of the EAC-1A regolith simulant.

The heat rate of the sintering protocol, and not only the temperature, is also expected to have an effect on the mechanical properties of the sintered objects. Here, a heat rate of 5 K/min was chosen for the initial drying and debinding steps. The choice of this heat rate was motivated by reported heat rates for sintering of regolith material found in the literature [21, 22]. Decreasing the heat rate during sintering will allow for a more uniform heating and cooling of the object, which in turn reduces the risk of crack formations during sintering due to temperature gradients in the material, as regions in the material closer to the outer surface will heat faster and have a higher temperature and therefore expand more than regions within the material with a lower temperature. This expansion will be according to the coefficient of thermal expansion for the material. It might be beneficial to the mechanical strength of the objects to reduce the heat rate even further than what was done in this work, although there is likely to be a trade-off between mechanical strength and considerations associated with an increased processing time such as cost and practicability.

The heterogeneous composition of regolith should also be noted here, and it can be expected that compounds having a relatively lower melting temperature such as Na₂O and Fe₂O₃ will start to sinter before compounds such as Al₂O₃, MgO and CaO. It should also be expected that the compounds will interact during the sintering procedure, giving rise to a more complex behaviour than what is otherwise observed when the melting behaviour for each compound is studied on its own. Compounds – or additives – in the material, having a lower melting temperature than that of the rest of the matrix, could give rise to liquid phase sintering of the material, which in turn might facilitate the densification of a porous sample as the liquid phase is able to penetrate voids in the sample which facilitates the mass transport during the sintering.

4.4. SEM

The SEM analysis was performed on the cross section of a sintered rectangular sample manufactured using the ‘LA’ concentration of sodium alginate. Figure 8 display a low-magnification image of the sample, illustrating the heterogeneous nature of the material: what can be seen are particles in a variety of shapes and sizes, the largest of them appearing to be about 200 µm. This would indicate that the slurry preparation step has the effect of reducing the upper particle size, as the grain size for the material is otherwise specified as being in the

range of 0.02–1 mm as mentioned previously. A sieved fraction of EAC-1A would reduce the initial upper size limit of the material further, meaning more homogeneous particle sizes in the sample as the total range of particle sizes is reduced.

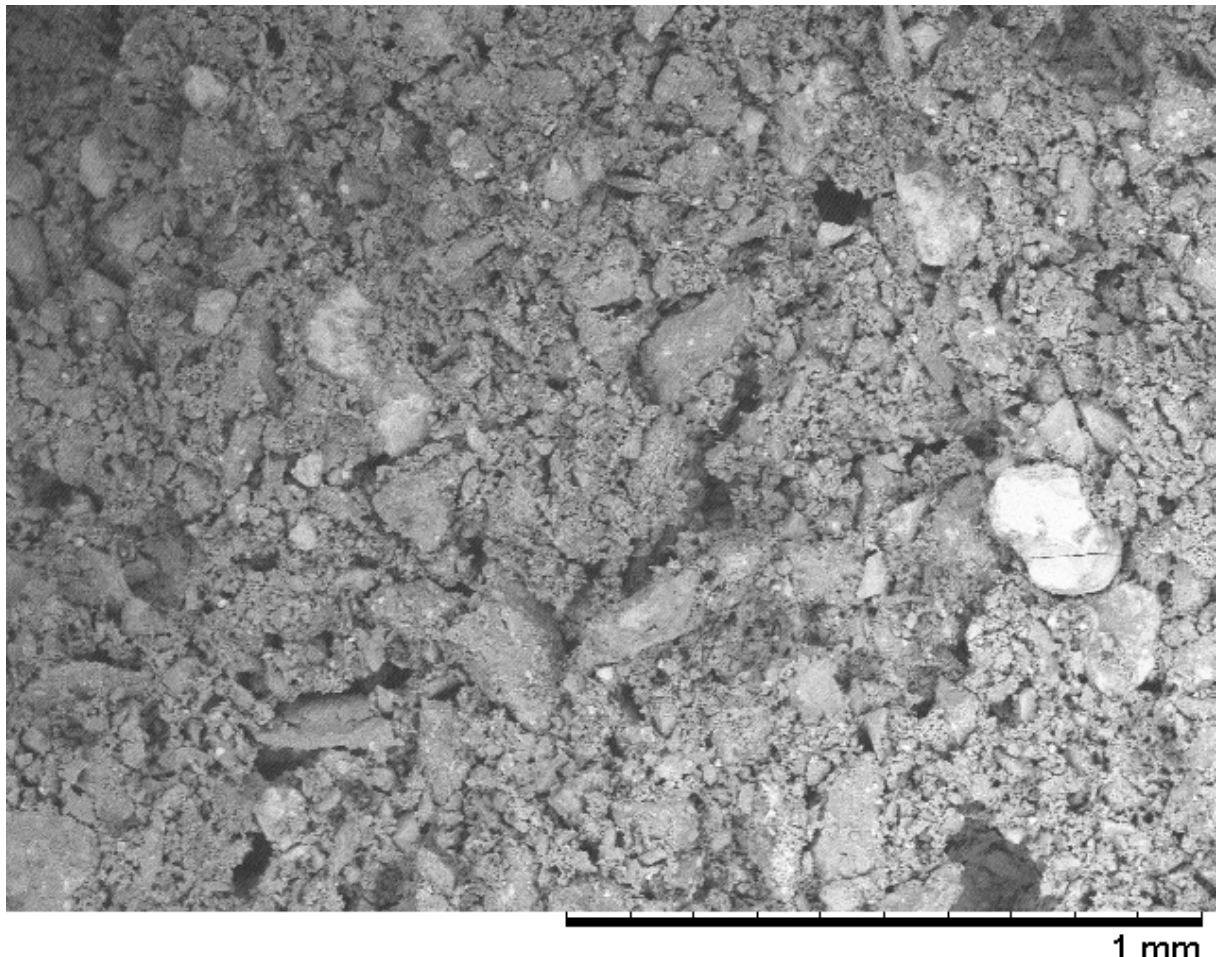


Figure 8. Image of cross section of sintered sample at x100 magnification.

What can also be observed is the high porosity – i.e. the low degree of particle close packing – in the sample, which can further be seen in Figure 9 taken at a higher magnification. Again, a large spread in particle sizes and shapes is observed, and the sample may be classified as being highly porous due to the significant amount of void space between particles as seen in the figure. It is possible that a finer particle size of the material than what is used here would allow a higher degree of close packing of particles, reducing the space between particles which in turn would facilitate sintering as discussed previously. Furthermore, an increase in solid phase during slurry preparation – i.e. a reduced water content – might lead to a denser sample, as the void volume that is observed here is likely to previously have been occupied by the gel-phase that is evaporated during the drying and the sintering stages.

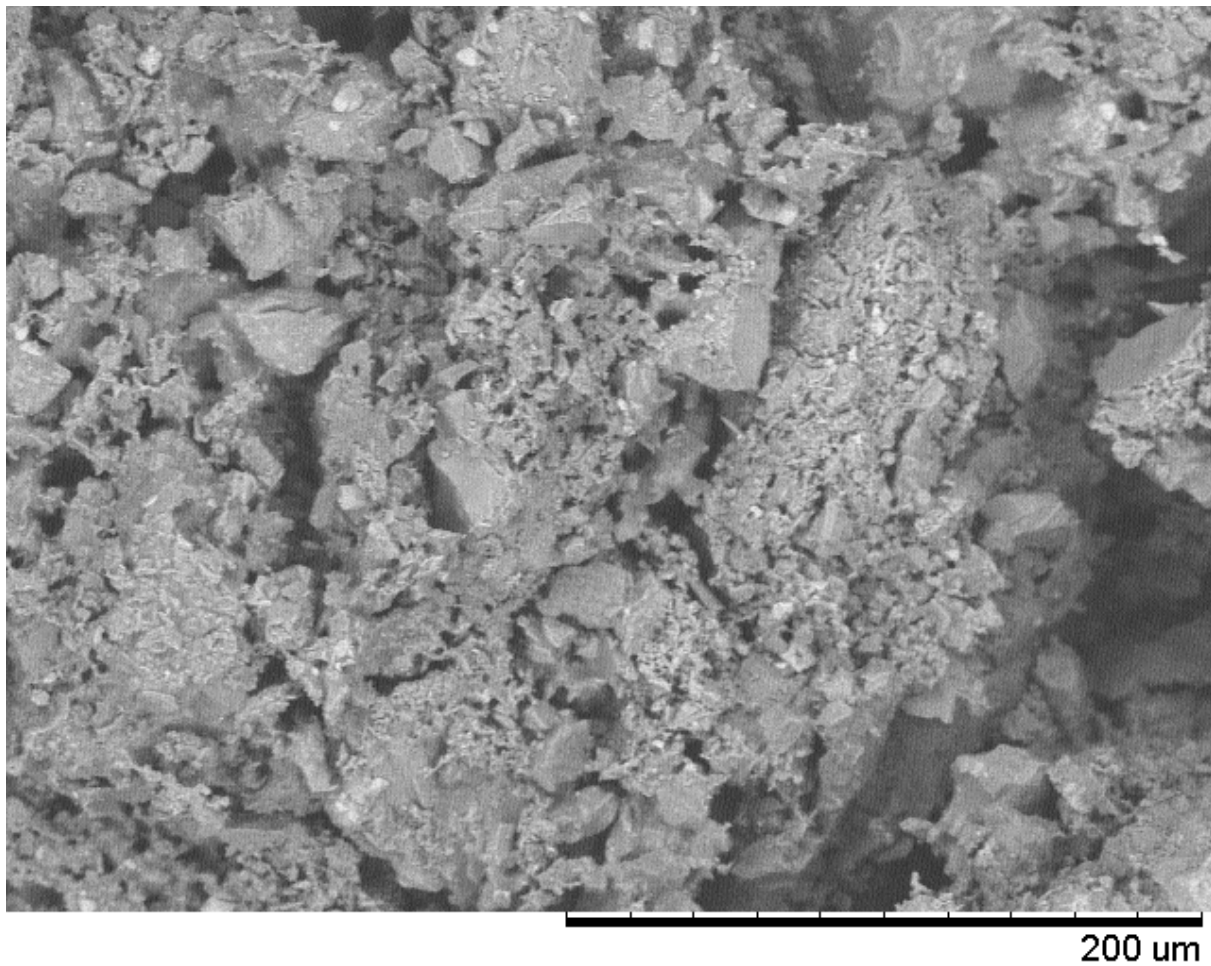


Figure 9. SEM image of sample at x500 magnification.

In Figure 10, jagged particle shapes throughout the sample can be observed; it is not clear whether this is a result of the slurry preparation step, or a property of the stock material, even though it is reasonable to believe that the pestling during the slurry preparation will influence particle morphology. The average sphericity Φ for the material has been reported as being in the range 0.59–0.60 Φ , where a sphere equals unity, indicating a moderate sphericity for the stock material [53].

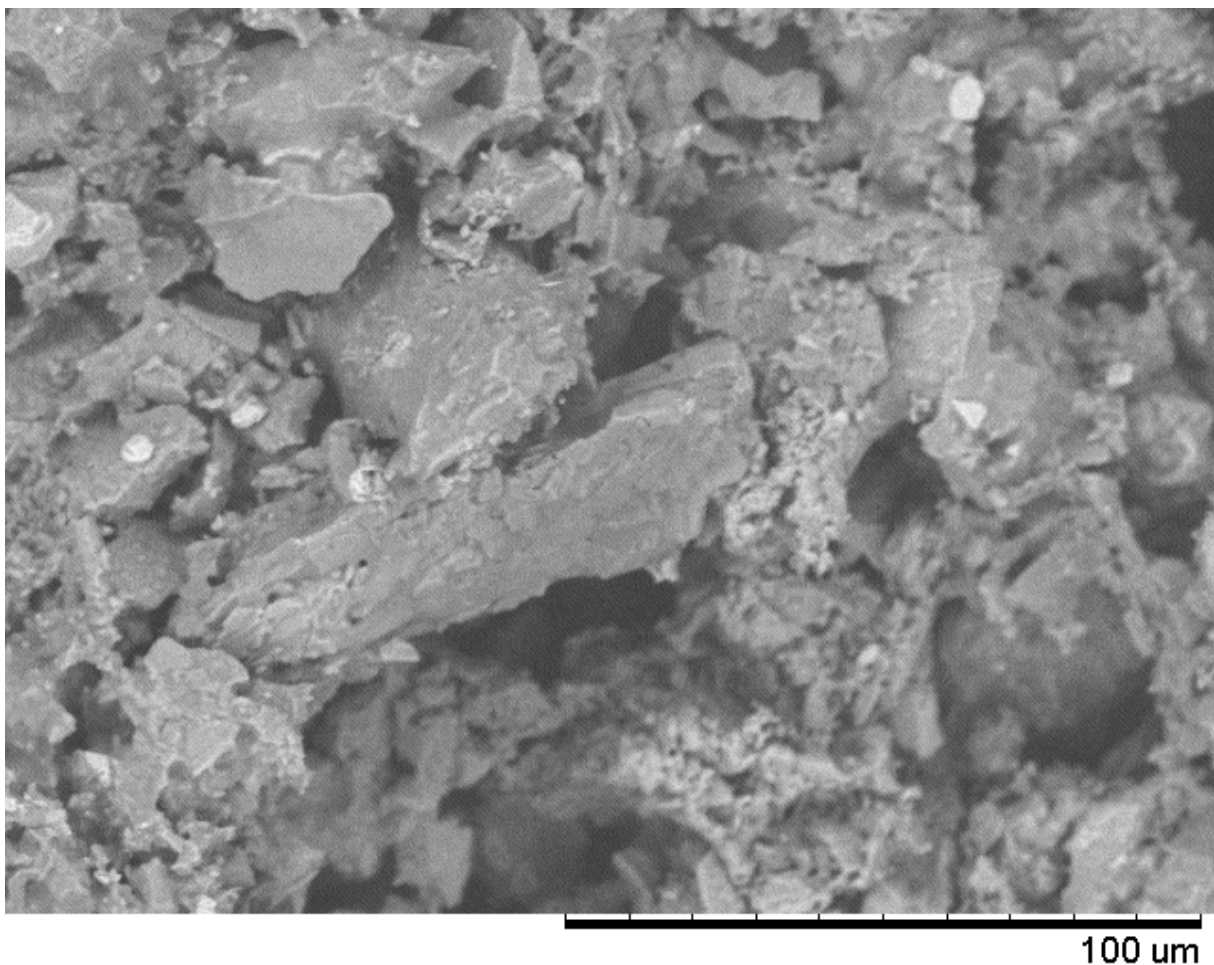


Figure 10. SEM image of sample cross section at x1000 magnification.

4.5. Compression testing

Sintered solid cylinder samples such as the one shown in Figure 7 above were used for compression testing. Four samples with an average diameter of 18.5 mm and an average height of 14.6 mm were tested. During the initial phase of the test, the load was concentrated on surface irregularities on the top of the samples; as these gave way, the load was spread evenly over the top surface of the cylinder. Before the recorded maximum load of each test, cracks were observed that propagated throughout the samples.

The average value for the compressive strength of the samples was recorded to be 2.4 MPa with a standard deviation of 0.2 MPa. Comparing with the values in Table 1, the compressive strength in this work is about one order of magnitude less than what is commonly reported. As have been discussed previously, it is believed that a less-than-optimal sintering was achieved during this work, which would explain the low value for compressive strength.

5. Conclusions

In this work, a new approach to additive manufacturing using regolith simulant as feedstock has been investigated in the form of the direct ink writing process, in which an extrudable dispersion is prepared together with regolith simulant in combination with water and a binding additive, all of which could be made available in the future for ISRU on the Moon. Two such binding additives were identified – sodium alginate and methyl cellulose – and the feasibility of the DIW process was demonstrated through the manufacture of objects with varying geometries.

It is believed that a non-ideal sintering process was carried out in this work, as the reported compressive strength of cylindrical objects were about one order of magnitude less than what is typically reported in the literature for sintered regolith samples. This is supported by the results from the SEM analysis, showing a highly porous inner structure of the sintered samples. It is suggested that the lunar regolith simulant used for this work – EAC-1A with a grain size distribution ranging between 0.02–1 mm – is to be sintered at 1100 °C for at least 2 h.

To conclude, the direct ink writing additive manufacturing process as studied here is a possible technology candidate for future lunar ISRU. The mechanical strength of components prepared with the method must first be improved, but it is not unreasonable to believe based on the results from this report that this can be achieved by using sieved regolith with a finer particle size distribution and by further optimising the sintering process. An advantage with the method studied here compared to the transport of construction material from Earth is that the two major dispersion components – regolith and water – are available as resources on the Moon, and that the third – either sodium alginate or methyl cellulose – in principle could be produced *in-situ* as well. All the extrusion based AM processes mentioned in Section 2.1 makes use of some kind of binder phase or additive – may it be phosphoric acid, mineral salts, urea or synthetic chemicals – that must be produced or resourced in some way, and a benefit of the additives studied in this work is their relative low toxicity and their ease of handling. Furthermore, only a small amount of binding agent – i.e. in the order of 1 wt.% – is needed to produce a viscous, printable ink, which is an additional benefit of this method compared to other methods requiring more additive.

As we humans progressively travel further away from Earth, the need to use local resources as raw materials will increase. Considering this, the topic of *in-situ* resource utilisation is and will be of utmost importance and relevance in the coming decades, as our plans to establish settlements on the Moon and, eventually, on Mars are turned into reality. It might prove to be

beneficial – and even necessary – to reevaluate ‘waste products’ such as carbon dioxide and food leftovers as being important assets that can be reinserted into the material streams, transforming them into valuable resources. Such initiatives might also inspire us to take a similar approach back on Earth, to help reduce the strain that a growing population and an increased material turnover inevitably will put on the planet.

6. Future work

It is suggested that future work on this topic addresses the following points:

- That experiments are carried out to establish optimal solid loading of regolith simulant in the dispersion to minimise self-buckling of structures.
- To establish the effect, if any, of additive concentration on the mechanical properties of samples, and if the mechanical properties differ depending on which additive is used.
- That the 3D printer is upgraded with a leadscrew driven Z-axis for improved accuracy, and also that the extruder motor is replaced with a stepper motor having higher torque to enable the use of finer nozzles and thus achieving higher resolution; another option would be to switch the extrusion system to a pneumatic one to reduce the mass carried by the printhead. Furthermore, the system may additionally be improved by adding a way to position the nozzle before each print in a calibrated manner, e.g. by installing an inductive sensor that responds to a target on the build plate.
- To identify a slicer software that is compatible with the process as it is described in this work, to allow for the direct use of CAD files enabling more complex geometries.
- That sintering is carried out at higher temperatures to establish the sintering behaviour and optimal process parameters for the regolith simulant EAC-1A with the grain sizes used for this work. The porosity of the samples should ideally be measured before and after sintering, and it may be insightful if the compressive strength of the samples is presented as a function of the sample porosity.

Acknowledgements

I am grateful to the staff at ESA for their support and for giving me this opportunity. I wish to thank Timon Schild at the European Astronaut Centre for his assistance, in particular relating to setting up the hardware of the 3D printer and for giving his feedback on the manuscript of this work. I would like to thank Wei Xia at Uppsala University for making the compression testing and SEM analysis possible.

References

1. Anand M, Crawford IA, Balat-Pichelin M, et al (2012) A brief review of chemical and mineralogical resources on the Moon and likely initial in situ resource utilization (ISRU) applications. *Planet Space Sci* 74:42–48.
<https://doi.org/10.1016/j.pss.2012.08.012>
2. Sherwood B (2019) Principles for a practical Moon base. *Acta Astronaut* 160:116–124.
<https://doi.org/10.1016/j.actaastro.2019.04.018>
3. Montes C, Broussard K, Gongre M, et al (2015) Evaluation of lunar regolith geopolymers binder as a radioactive shielding material for space exploration applications. *Adv Sp Res* 56:1212–1221. <https://doi.org/10.1016/j.asr.2015.05.044>
4. Hinterman E (2020) Simulating oxygen production on Mars for the Mars Oxygen In-Situ Resource Utilization Experiment. *Acta Astronaut* 170:678–685.
<https://doi.org/10.1016/j.actaastro.2020.02.043>
5. Nieke P, Kita J, Häming M, Moos R (2019) Manufacturing dense thick films of lunar regolith simulant EAC-1 at room temperature. *Materials (Basel)* 12:.
<https://doi.org/10.3390/ma12030487>
6. Schleppi J, Gibbons J, Groetsch A, et al (2019) Manufacture of glass and mirrors from lunar regolith simulant. *J Mater Sci* 54:3726–3747. <https://doi.org/10.1007/s10853-018-3101-y>
7. Song L, Xu J, Fan S, et al (2019) Vacuum sintered lunar regolith simulant: Pore-forming and thermal conductivity. *Ceram Int* 45:3627–3633.
<https://doi.org/10.1016/j.ceramint.2018.11.023>
8. Schlördt T, Schwanke S, Keppner F, et al (2013) Robocasting of alumina hollow filament lattice structures. *J Eur Ceram Soc* 33:3243–3248.
<https://doi.org/10.1016/j.jeurceramsoc.2013.06.001>
9. Taylor SL, Jakus AE, Shah RN, Dunand DC (2017) Iron and Nickel Cellular Structures by Sintering of 3D-Printed Oxide or Metallic Particle Inks. *Adv Eng Mater* 19:.
<https://doi.org/10.1002/adem.201600365>
10. Jakus AE, Taylor SL, Geisendorfer NR, et al (2015) Metallic Architectures from 3D-Printed Powder-Based Liquid Inks. *Adv Funct Mater* 25:6985–6995.
<https://doi.org/10.1002/adfm.201503921>
11. ISO/ASTM (2015) INTERNATIONAL STANDARD ISO / ASTM 52900 Additive manufacturing — General principles — Terminology. *Int Organ Stand*.

- <https://doi.org/10.1520/ISOASTM52900-15>
12. Lewis JA, Smay JE, Stuecker J, Cesarano J (2006) Direct ink writing of three-dimensional ceramic structures. *J Am Ceram Soc* 89:3599–3609.
<https://doi.org/10.1111/j.1551-2916.2006.01382.x>
13. Dai L, Cheng T, Duan C, et al (2019) 3D printing using plant-derived cellulose and its derivatives: A review. *Carbohydr Polym* 203:71–86.
<https://doi.org/10.1016/j.carbpol.2018.09.027>
14. Colaprete A, Schultz P, Heldmann J, et al (2010) Detection of water in the LCROSS ejecta plume. *Science* (80-) 330:463–468. <https://doi.org/10.1126/science.1186986>
15. Way JC, Silver PA, Howard RJ (2011) Sun-driven microbial synthesis of chemicals in space. *Int J Astrobiol* 10:359–364. <https://doi.org/10.1017/S1473550411000218>
16. Menezes AA, Cumbers J, Hogan JA, Arkin AP (2015) Towards synthetic biological approaches to resource utilization on space missions. *J R Soc Interface* 12:.
<https://doi.org/10.1098/rsif.2014.0715>
17. National Research Council (2014) 3D Printing in Space. National Academies Press, Washington, D.C.
18. Williams H, Butler-Jones E (2019) Additive manufacturing standards for space resource utilization. *Addit Manuf* 28:676–681.
<https://doi.org/10.1016/j.addma.2019.06.007>
19. Wilhelm S, Curbach M (2014) Review of possible mineral materials and production techniques for a building material on the moon. *Struct Concr* 15:419–428.
<https://doi.org/10.1002/suco.201300088>
20. Buchner C, Pawelke RH, Schlauf T, et al (2018) A new planetary structure fabrication process using phosphoric acid. *Acta Astronaut* 143:272–284.
<https://doi.org/10.1016/j.actaastro.2017.11.045>
21. Zocca A, Fateri M, Al-Sabbagh D, Günster J (2020) Investigation of the sintering and melting of JSC-2A lunar regolith simulant. *Ceram Int* 0–1.
<https://doi.org/10.1016/j.ceramint.2020.02.212>
22. Taylor SL, Jakus AE, Koube KD, et al (2018) Sintering of micro-trusses created by extrusion-3D-printing of lunar regolith inks. *Acta Astronaut* 143:1–8.
<https://doi.org/10.1016/j.actaastro.2017.11.005>
23. Indyk SJ, Benaroya H (2017) A structural assessment of unrefined sintered lunar regolith simulant. *Acta Astronaut* 140:517–536.
<https://doi.org/10.1016/j.actaastro.2017.09.018>

24. Gualtieri T, Bandyopadhyay A (2015) Compressive deformation of porous lunar regolith. *Mater Lett* 143:276–278. <https://doi.org/10.1016/j.matlet.2014.11.153>
25. Chow BJ, Chen T, Zhong Y, Qiao Y (2017) Direct Formation of Structural Components Using a Martian Soil Simulant. *Sci Rep* 7:1–8. <https://doi.org/10.1038/s41598-017-01157-w>
26. Liu M, Tang W, Duan W, et al (2019) Digital light processing of lunar regolith structures with high mechanical properties. *Ceram Int* 45:5829–5836. <https://doi.org/10.1016/j.ceramint.2018.12.049>
27. Revelo CF, Colorado HA (2018) 3D printing of kaolinite clay ceramics using the Direct Ink Writing (DIW) technique. *Ceram Int* 44:5673–5682. <https://doi.org/10.1016/j.ceramint.2017.12.219>
28. Hensen TJ, Aguirre TG, Cramer CL, et al (2018) Additive manufacturing of ceramic nanopowder by direct coagulation printing. *Addit Manuf* 23:140–150. <https://doi.org/10.1016/j.addma.2018.07.010>
29. Revelo CF, Colorado HA (2019) 3D printing of kaolinite clay with small additions of lime, fly ash and talc ceramic powders. *Process Appl Ceram* 13:287–299. <https://doi.org/10.2298/PAC1903287R>
30. Perrot A, Rangeard D, Courteille E (2018) 3D printing of earth-based materials: Processing aspects. *Constr Build Mater* 172:670–676. <https://doi.org/10.1016/j.conbuildmat.2018.04.017>
31. Cesaretti G, Dini E, De Kestelier X, et al (2014) Building components for an outpost on the Lunar soil by means of a novel 3D printing technology. *Acta Astronaut* 93:430–450. <https://doi.org/10.1016/j.actaastro.2013.07.034>
32. Pilehvar S, Arnhof M, Pamies R, et al (2020) Utilization of urea as an accessible superplasticizer on the moon for lunar geopolymmer mixtures. *J Clean Prod* 247:. <https://doi.org/10.1016/j.jclepro.2019.119177>
33. Jakus AE, Koube KD, Geisendorfer NR, Shah RN (2017) Robust and Elastic Lunar and Martian Structures from 3D-Printed Regolith Inks. *Sci Rep* 7:1–8. <https://doi.org/10.1038/srep44931>
34. Caprio L, Demir AG, Previtali B, Colosimo BM (2020) Determining the feasible conditions for processing lunar regolith simulant via laser powder bed fusion. *Addit Manuf* 32:101029. <https://doi.org/10.1016/j.addma.2019.101029>
35. Goulas A, Harris RA, Friel RJ (2016) Additive manufacturing of physical assets by using ceramic multicomponent extra-terrestrial materials. *Addit Manuf* 10:36–42.

- https://doi.org/10.1016/j.addma.2016.02.002
36. Xu J, Cao H, Sun X, et al (2019) 3D printing of hypothetical brick by selective laser sintering using lunar regolith simulant and ilmenite powders. *1084208:9*.
<https://doi.org/10.1117/12.2505911>
37. Goulas A, Friel RJ (2016) 3D printing with moondust. *Rapid Prototyp J* 22:864–870.
<https://doi.org/10.1108/RPJ-02-2015-0022>
38. Fateri M, Gebhardt A (2015) Process parameters development of selective Laser Melting of lunar regolith for on-site manufacturing applications. *Int J Appl Ceram Technol* 12:46–52. <https://doi.org/10.1111/ijac.12326>
39. Balla VK, Roberson LB, O'Connor GW, et al (2012) First demonstration on direct laser fabrication of lunar regolith parts. *Rapid Prototyp J* 18:451–457.
<https://doi.org/10.1108/13552541211271992>
40. Allan S, Braunstein J, Baranova I, et al (2013) Computational modeling and experimental microwave processing of JSC-1A lunar simulant. *J Aerosp Eng*.
[https://doi.org/10.1061/\(ASCE\)AS.1943-5525.0000245](https://doi.org/10.1061/(ASCE)AS.1943-5525.0000245)
41. Meurisse A, Makaya A, Willsch C, Sperl M (2018) Solar 3D printing of lunar regolith. *Acta Astronaut* 152:800–810. <https://doi.org/10.1016/j.actaastro.2018.06.063>
42. Toutanji HA, Evans S, Grugel RN (2012) Performance of lunar sulfur concrete in lunar environments. *Constr Build Mater* 29:444–448.
<https://doi.org/10.1016/j.conbuildmat.2011.10.041>
43. Faierson EJ, Logan K V., Stewart BK, Hunt MP (2010) Demonstration of concept for fabrication of lunar physical assets utilizing lunar regolith simulant and a geothermite reaction. *Acta Astronaut* 67:38–45. <https://doi.org/10.1016/j.actaastro.2009.12.006>
44. Dove CA, Bradley FF, Patwardhan S V. (2016) Seaweed biopolymers as additives for unfired clay bricks. *Mater Struct Constr* 49:4463–4482.
<https://doi.org/10.1617/s11527-016-0801-0>
45. Liu Q, Li Q, Xu S, et al (2018) Preparation and properties of 3D printed alginate-chitosan polyion complex hydrogels for tissue engineering. *Polymers (Basel)* 10:.
<https://doi.org/10.3390/polym10060664>
46. Pusch K, Hinton TJ, Feinberg AW (2018) Large volume syringe pump extruder for desktop 3D printers. *HardwareX* 3:49–61. <https://doi.org/10.1016/j.ohx.2018.02.001>
47. Bruice PY (2016) Essential Organic Chemistry, 3rd ed. Pearson
48. Peacock, Andrew J.; Calhoun A (2007) Polymer chemistry: properties and applications. *Choice Rev Online* 44:44-3878-44–3878.

- https://doi.org/10.5860/choice.44-3878
49. Skjåk-Bræk G, Draget KI (2012) Alginates: Properties and Applications. Elsevier B.V.
 50. Tang S, Yang L, Li G, et al (2019) 3D printing of highly-loaded slurries via layered extrusion forming: Parameters optimization and control. *Addit Manuf* 28:546–553. <https://doi.org/10.1016/j.addma.2019.05.034>
 51. Schubert U, Hüsing N (2019) Synthesis of Inorganic Materials, 4th ed. Wiley
 52. Callister WD, Rethwisch DG (2014) Materials Science and Engineering, 9th ed. Wiley
 53. Engelschiøn VS, Eriksson SR, Cowley A, et al (2020) EAC-1A: A novel large-volume lunar regolith simulant. *Sci Rep* 10:1–9. <https://doi.org/10.1038/s41598-020-62312-4>
 54. Hart KR, Frketic JB, Brown JR (2018) Recycling meal-ready-to-eat (MRE) pouches into polymer filament for material extrusion additive manufacturing. *Addit Manuf* 21:536–543. <https://doi.org/10.1016/j.addma.2018.04.011>
 55. Rueschhoff L, Costakis W, Michie M, et al (2016) Additive Manufacturing of Dense Ceramic Parts via Direct Ink Writing of Aqueous Alumina Suspensions. *Int J Appl Ceram Technol* 13:821–830. <https://doi.org/10.1111/ijac.12557>

Appendix

The Python script below was written for Python 3.8.3 and can be used to generate G-code for selected geometries by uncommenting one of the seven function calls at the end of the code. The code has only been tested for a limited set of parameters, and any modifications to it may result in unexpected behaviour.

```
#import sys # uncomment together with line "sys.stdout" to create gcode file from print output

def Circular_motion(radius, e_feedrate): # clockwise circular arc
    print('G2 I', round(radius, 1), ' E', round(Circumference(
        radius) * e_feedrate, 4), sep='') # I = radius or distance to center

def Circumference(radius): # calculate circumference of circle
    c = radius * 2 * 3.141593
    return c

def Cone(): # creates cone shape of stacked circles
    Print_begin() # sets printhead before job
    radius = 8 # in mm
    step_size = 0.2 # sets radius change for next layer in mm
    b = step_size # counter
    x_coordinates = []
    for x in range(2, nr_layers+2):
        x_coordinates.append(20 + b) # change to + for decrease and - for increase
        b = step_size * x
```

```

for x in range(0, nr_layers):
    Circular_motion(radius, e_feedrate)
    Z_lift(layer_height)
    print('G1 X', x_coordinates[x], sep='')
    radius = round(radius - step_size, 1) # change to - for decrease and + for increase
Print_finish() # sets printhead after job

def Cylinder():
    Print_begin() # sets printhead before job
    radius = 10 # max allowed radius
    i = [] # list with radii of circles
    i.append(1) # radius of smallest circle
    b = 2 # used as counter
    subtract_lst = [] # to adjust radius
    x_start = 20
    for y in range(1, int(radius/2) + 3, 2):
        i.append(y + 2)
    for x in range(0, len(i)):
        subtract_lst.append(round(x * 0.1, 1))
    for number in range(0, nr_layers):
        if(number % 2 == 0): # for even layers, starting with the first
            for x in range(0, len(i)): # circles going inward out
                print('G1 X', x_start + b - i[x] + subtract_lst[x], '\nG2 I', i[x] - subtract_lst[x], ' E',
                      round(Circumference(i[x])) * e_feedrate, 4), sep='')
        if(number % 2 != 0): # for uneven layers, starting with the second
            for x in reversed(range(0, len(i))): # circles going outward in
                print('G1 X', x_start + b - i[x] + subtract_lst[x], '\nG2 I', i[x] - subtract_lst[x], ' E',
                      round(Circumference(i[x])) * e_feedrate, 4), sep='')
            Z_lift(layer_height)
    Print_finish() # sets printhead after job

def Dome(): # creates dome shape of stacked circles
    Print_begin() # sets printhead before job
    radius = 8 # in mm
    step_size = 0.1 # sets radius change for next layer in mm
    x_coordinates = [20] * (nr_layers + 1)
    counter_lst = [0] * (nr_layers + 1)
    for x in range(1, nr_layers+1): # sets how fast the top decreases
        counter_lst[x] = round(step_size * x, 1)
        step_size = step_size + 0.005
        x_coordinates[x] = x_coordinates[x-1] + counter_lst[x]
    for x in range(0, nr_layers):
        Circular_motion(radius, e_feedrate)
        Z_lift(layer_height)
        print('G1 X', round(x_coordinates[x], 1), sep='')
        radius = round(radius - counter_lst[x], 1)
    Print_finish() # sets printhead after job

def Lattice():
    Print_begin()
    X_start = 20

```

```

Y_start = 20
lattice_spacing = 4 # mm spacing between toolpaths
length = 28
lattice_start = Y_start
Y_counter = int(lattice_start + lattice_spacing)
end = int((X_start + length - lattice_spacing + nozzle_width_half + 7))
y_extr = ((lattice_spacing + nozzle_width_half) * e_feedrate)
x_extr = round(((end - X_start) * e_feedrate), 3)
x_lst = []
x_lst.append(X_start)
x_lst.append(end)
for number in range(0, nr_layers):
    if(number % 2 == 0):
        count = -1
        for __ in range(0, int(length/lattice_spacing)):
            print('G1 Y', x_lst[count], ' E', x_extr,
                  '\nG1 X', Y_counter, ' E', y_extr, sep='')
            Y_counter = Y_counter + lattice_spacing
            count = (count + 1) % 2
        print('G1 Y', x_lst[0], ' E', x_extr, '\nG1 X', Y_counter, ' E', y_extr,
              '\nG1 Y', x_lst[-1], ' E', x_extr, sep='')
    if(number % 2 != 0):
        for __ in range(0, int(length/lattice_spacing)):
            Y_counter = Y_counter - lattice_spacing
            print('G1 X', x_lst[count], ' E', x_extr,
                  '\nG1 Y', Y_counter, ' E', y_extr, sep='')
            count = (count + 1) % 2
        print('G1 X', x_lst[count], ' E', x_extr, sep='')
        print('G1 Y', Y_counter - lattice_spacing, ' E',
              y_extr, '\nG1 X', x_lst[0], ' E', x_extr, sep='')
    Z_lift(layer_height)
Print_finish()

def Print_begin():
    # to be run at start of print. Lifts Z-axis and moves X, Y to start position
    # G91 = all axes relative. G1 = linear move.
    print('G91\nG1 Z', layer_height, '\nG90\nM83\nM207 Z1 S2\nM203 E1 X7 Y7\nG1 E0.15',
          '\nG1 X15 Y15\nM83\nG1 X20 Y20\nG1 E0.50\nG4 P1000', sep='')

def Print_finish():
    # to be run at end of print. Lifts Z-axis and moves X, Y
    # G10 = retract according to setting in M207. G91 = all axes relative. G1 = linear move.
    # G90 = all axes absolute. G4 = pause (dwell) for P milliseconds.
    print('G10\nG91\nG1 Z', round(layer_height * 3, 1),
          '\nG90\nM83\nG1 X10 Y10\nG1 X0 Y0 E1', sep='')

def Rectangle(): # creates rectangle
    Print_begin() # sets printhead before job
    rectangle_length = 20 # in mm, along x
    rectangle_width = 12 # in mm, along y
    while(rectangle_width % 4 != 0): # ensures correct coordinates after z lift

```

```

    rectangle_width = rectangle_width + 1
x_start = 20
y_start = 20
x_coordinates = []
x_coordinates.append(x_start)
x_coordinates.append(x_start + rectangle_length) # extrusion in mm along length
e_x = round(e_feedrate * (x_coordinates[-1] - x_coordinates[0]), 3)
e_y = round(e_feedrate * nozzle_width, 3) # extrusion in mm along width
y_counter = y_start + nozzle_width # width coordinate counter (per step)
for number in range(0, nr_layers): # loop number of layers
    count = -1 # used to alternate between last and first value in x_coordinates
    if(number % 2 == 0): # for even layers, starting with the first
        if y_counter != y_start + nozzle_width: # used to reset value when more than two layers
            y_counter = y_start + nozzle_width
        for __ in range(1, int(rectangle_width/nozzle_width) + 1):
            print('G1 X', x_coordinates[count], ' E', e_x, sep='')
            print('G1 Y', round(y_counter, 1), ' E', e_y, sep='')
            y_counter = y_counter + nozzle_width
            count = (count + 1) % 2
    if(number % 2 != 0): # for uneven layers, starting with the second
        y_counter = y_counter - nozzle_width
        count = 0
        for __ in range(1, int(rectangle_width/nozzle_width) + 1):
            y_counter = y_counter - nozzle_width
            print('G1 X', x_coordinates[count], ' E', e_x, sep='')
            print('G1 Y', round(y_counter, 1), ' E', e_y, sep='')
            count = (count + 1) % 2
    print('G1 X', x_coordinates[count], ' E', e_x, sep='')
    Z_lift(layer_height) # lifts z
Print_finish() # sets printhead after job

def Rocket():
    radius = 6 # in mm
    later_radius = 0
    step_size = 0.4 # sets radius change for next layer in mm
    leg_decrease = 0
    x_start = 20
    y_start = 20
    circle_coordinates = []
    circle_coordinates.append(4.916) # can be estimated using y=1.0439x-1.326 where x is radius of first circle
    leg_length = 20 # in mm
    coordinate = [0] * 5
    coordinate[0] = y_start - nozzle_width_half
    coordinate[1] = x_start - radius
    print('G91\nG1 Z', layer_height, '\nG90\nM83\nM207 F4000 S3 Z2\nM203 E1 X7 Y7\nG1 E0.2', # sets printhead
before job
        '\nG1 X15 Y15\nM83\nG1 X20 Y20', sep='')
    print('G1 Y', round(coordinate[0], 1), '\nG1 X', round(
        coordinate[1], 1), '\nG1 E0.30\nG4 P500', sep='')
    for x in range(0, 6): # 1st portion, with legs
        coordinate[0] = x_start - leg_length + leg_decrease # 1st leg

```

```

coordinate[1] = y_start + nozzle_width_half
coordinate[2] = x_start - radius
coordinate[3] = coordinate[1] + circle_coordinates[0]
coordinate[4] = coordinate[2] + circle_coordinates[0]
print('G1 X', coordinate[0], ' E', round(
    e_feedrate * (coordinate[2] - coordinate[0]), 3), sep='')
print('G1 Y', coordinate[1], ' E', round(
    e_feedrate * nozzle_width, 3), sep='')
print('G1 X', round(coordinate[2], 1), ' E', round(
    e_feedrate * (coordinate[2] - coordinate[0]), 3), sep='')
print('G2 E', round(e_feedrate * Circumference(radius)/4, 3), ' X',
      coordinate[4], ' Y', round(coordinate[3], 1), ' R', round(radius, 1), sep='')
coordinate[0] = coordinate[1] + circle_coordinates[0] + \
    leg_length - radius - leg_decrease # 2nd leg
coordinate[1] = coordinate[2] + circle_coordinates[0] + nozzle_width
coordinate[2] = coordinate[0] - leg_length + radius + leg_decrease
print('G1 Y', round(coordinate[0], 1), ' E', round(e_feedrate * (coordinate[0] - coordinate[2]), 3),
      '\nG1 X', round(coordinate[1], 1), ' E', round(
          e_feedrate * nozzle_width, 3), '\nG1 Y', round(coordinate[2], 1),
      ' E', round(e_feedrate * (coordinate[0] - coordinate[2]), 3), sep='')
print('G2 E', round(e_feedrate * (Circumference(radius)/4), 3), ' X', round(coordinate[1] +
circle_coordinates[0], 1),
      ' Y', round(coordinate[2] - circle_coordinates[0], 1), ' R', round(radius, 1), sep='')
coordinate[0] = coordinate[1] + circle_coordinates[0] + \
    leg_length - radius - leg_decrease # 3rd leg
coordinate[1] = coordinate[2] - circle_coordinates[0] - nozzle_width
coordinate[2] = coordinate[0] - leg_length + radius + leg_decrease
coordinate[3] = coordinate[2] - circle_coordinates[0]
coordinate[4] = coordinate[1] - circle_coordinates[0]
print('G1 X', round(coordinate[0], 1), ' E', round(e_feedrate * (coordinate[0] - coordinate[2]), 3), '\nG1
Y',
      round(coordinate[1], 1), ' E', round(
          e_feedrate * nozzle_width, 3), '\nG1 X', round(coordinate[2], 1),
      ' E', round(e_feedrate * (coordinate[0] - coordinate[2]), 3), sep='')
print('G2 E', round(e_feedrate * (Circumference(radius)/4), 3), ' X', round(coordinate[3], 1), ' Y',
      round(coordinate[4], 1), ' R', round(radius, 1), sep='')
coordinate[0] = coordinate[4] - leg_length + \
    radius + leg_decrease # 4th leg
coordinate[1] = coordinate[3] - nozzle_width
coordinate[2] = coordinate[0] + leg_length - radius - leg_decrease
coordinate[3] = coordinate[1] - circle_coordinates[0]
coordinate[4] = coordinate[2] + circle_coordinates[0]
print('G1 Y', round(coordinate[0], 1), ' E', round(e_feedrate * (coordinate[2] - coordinate[0]), 3), '\nG1
X',
      round(coordinate[1], 1), ' E', e_feedrate *
      round(nozzle_width, 1), '\nG1 Y', round(coordinate[2], 1),
      ' E', round(e_feedrate * (coordinate[2] - coordinate[0]), 3), sep='')
print('G2 E', round(e_feedrate * (Circumference(radius)/4), 3), ' X', round(coordinate[3], 1), ' Y',
      round(coordinate[4], 1), ' R', round(radius, 1), sep='')
radius = radius + step_size
circle_coordinates[0] = circle_coordinates[0] + step_size

```

```

    Z_lift(layer_height)
    if x > 0:
        leg_decrease = leg_decrease + 1 # sets how fast the legs decrease in size
    coordinate[3] = coordinate[3] - 0.4
    print('G1 X', round(coordinate[3], 1), ' Y', y_start, sep='')
    step_size = 0.2
    for x in range(0, 7): # 2nd portion, without legs
        later_radius = 20 - coordinate[3] # 17.732 center point
        Circular_motion(later_radius, e_feedrate)
        coordinate[3] = round(coordinate[3] - step_size, 1)
        print('G1 X', coordinate[3], sep='')
        Z_lift(layer_height)
        later_radius = later_radius + step_size
    for x in range(0, 3): # 3rd portion, waist
        Circular_motion(later_radius, e_feedrate)
        print('G1 X', coordinate[3], sep='')
        Z_lift(layer_height)
        step_size = 0.05
    counter_lst = [0] * 16
    for x in range(1, int(13)+1): # sets how fast the top decreases
        counter_lst[x] = round(step_size * x, 1)
        step_size = step_size + 0.004
    for x in range(0, 14): # 4th portion, top
        later_radius = later_radius - counter_lst[x]
        Circular_motion(later_radius, e_feedrate)
        coordinate[3] = round(coordinate[3] + counter_lst[x], 1)
        print('G1 X', coordinate[3], sep='')
        Z_lift(layer_height)
    Print_finish() # sets printhead after job

def Stacked_circles(): # creates stacked circles
    Print_begin() # sets printhead before job
    radius = 10 # in mm
    for __ in range(0, nr_layers):
        Circular_motion(radius, e_feedrate)
        Z_lift(layer_height)
    Print_finish() # sets printhead after job

def Z_lift(layer_height):
    # lift Z-axis by z_height mm
    # G91 = all axes relative. G1 = linear move. G90 = all axes absolute. M83 = E-axis relative.
    print('G91\nG1 Z', layer_height, '\nG90\nM83', sep='')

#sys.stdout = open('output.gcode','wt') # uncomment together with line "import sys" to create gcode file from print output

nozzle_width = 2 # in mm
nozzle_width_half = int(nozzle_width / 2)
layer_height = 1.2 # in mm
total_height = 15 # in mm
nr_layers = int(total_height/layer_height)

```

```
e_feedrate = 0.004 # mm e feed per mm x, y travel

#Cone()
#Cylinder()
#Dome()
#Lattice()
#Rectangle()
#Rocket()
#Stacked_circles()
```